Crystal plane dependent dispersion of cobalt metal on metastable aluminas

Ilya V Yakovlev, Vladimir I Zaikovskii, Mariya A Kazakova, Evgeniy S Papulovskiy, Olga B Lapina, Jean-Baptiste d'Espinose de Lacaillerie

Crystal plane dependent dispersion of cobalt metal on metastable aluminas

Ilya V. Yakovlev,[a, b, c] Vladimir I. Zaikovskii,[b] Mariya A. Kazakova,[b] Evgeniy S. Papulovskiy,[b] Olga B. Lapina,[a, b] and Jean-Baptiste d'Espinose de Lacaillerie[c, *]

[a] Novosibirsk State University, Pirogova Street 1, 630090 Novosibirsk, Russia

[b] Boreskov Institute of Catalysis SB RAS, Prospekt Lavrentieva 5, 630090, Novosibirsk, Russia

[c] SIMM, UMR CNRS 7615, ESPCI Paris, Université PSL, Sorbonne Université, 10 Rue Vauquelin, 75005 Paris, France

[*] Corresponding author. Email address: jean-baptiste.despinose@espci.fr

Abstract

Metallic Co nanoparticles, widely used and studied as supported heterogeneous catalysts for Fischer-Tropsch synthesis (FTS), display catalytic properties that can vary significantly depending on their size and crystal structure. In this work, we used ^{59}Co Internal Field NMR (^{59}Co IF NMR) complemented by high-resolution transmission electron microscopy (HRTEM) to demonstrate the influence of strong metal-support interaction on two noticeably different metastable alumina phases - γ-Al_2O_3 and χ-Al_2O_3. According to ^{59}Co IF NMR and HRTEM, the metallic particles supported on χ-Al_2O_3 were larger and displayed a significantly higher content of Co in its *hcp* phase, which are known to be more active and selective to C_{5+} in FTS. The ^{1}H NMR chemical shifts of hydroxyl groups anchored to the (110) and (111) spinel crystal planes were calculated by DFT. It revealed that the hydroxyl coverage of γ-Al_2O_3 facilitates the dispersion of Co precursor over the surface of the support, ultimately leading to the formation of smaller metal Co nanoparticles on γ-Al_2O_3 than on χ-Al_2O_3.

Keywords: heterogeneous catalysis, ^{59}Co NMR, HRTEM, Internal Field NMR, DFT, metal support interaction, Fischer-Tropsch synthesis

1 Introduction

The catalytic properties of nanoparticles (NPs) strongly depend on their size, crystal structure and morphology – factors that have a complex interconnection with each other but that are, to some extent, controllable by adjusting the synthesis conditions. An important case study of this dependence is metallic cobalt supported on oxides whose catalytic behavior depends strongly on the metal-support interaction in ways that are not yet fully understood.[1] In Fischer-Tropsch synthesis (FTS) for example, the choice of the support as well as possible decorations with various noble metal promoters are used to control the morphology and crystal structure of cobalt NPs in order to obtain the desired catalytic properties. The influence of these two properties of cobalt NPs on activity and selectivity towards C_{5+} hydrocarbons has been extensively studied in the recent decades resulting in some generally agreed-upon requirements. First, vast experimental data [2–7] indicate that, between the two most common structures met in metallic cobalt, the hexagonal close-packed (*hcp*) crystal structure is more active and selective towards C_{5+} than the face-centered cubic (*fcc*) one. Second, experimental data and theoretical calculations show that below a certain size (between 4 and 10 nm according to different sources) cobalt NPs become much less active in FTS and their selectivity shifts to CH_4 [8–13]. However, in many instances, how the desired cobalt size and structure are tailored by the support remains an open question.

During the preparation step, how the support directs the speciation of Co(II) ions and complexes from the precursor has been efficiently investigated by spectroscopic means (noticeably UV-visible spectroscopy[14] and EXAFS[15]), rationalized through coordination chemistry[16] and modeled by DFT.[17] Nevertheless, the interaction of the support with the larger Co nanoparticles obtained after reduction is paradoxically more difficult to characterize or model.[18]

Co nanoparticles can be characterized by a variety of physical methods: X-Ray diffraction (XRD), electron microscopy techniques (transmission, scanning, or scanning transmission), magnetometry, magnetic resonance techniques (electronic ferromagnetic resonance - FMR, ^{59}Co Internal Field nuclear magnetic resonance – IF NMR). All of these techniques have their own experimental limitations and provide different kinds of structural information. In this work, we rely on a combination of ^{59}Co Internal Field NMR (^{59}Co IF NMR) and high-resolution transmission electron microscopy (HRTEM), a combination that proved effective in some of our previous works.[19–22] HRTEM is an indispensable technique providing unique information on the morphology of the particles close to the single-atom scale. However, the intrinsic limitation of this technique is its local character, making it necessary to extrapolate the data obtained from

a limited set of micrographs. ^{59}Co IF NMR, on the contrary, is a bulk technique that was shown to provide information on the crystal and magnetic structures of Co nanoparticles [19,20,23–26] as well as on their size distribution,[21,27] even though it is limited by the intrinsically low intensity of the NMR signal and the difficulty of spectral analysis.

We focus here on the role of two low-temperature metastable alumina phases, γ-Al_2O_3 and χ-Al_2O_3, in directing the dispersion and structure of Co nanoparticles. γ-Al_2O_3 is a well-studied and widely employed support in Co FTS catalysts. It has a high specific surface area and demonstrates good stability under usual reaction conditions when stabilized by metal oxides. χ-Al_2O_3 is the lowest temperature form of alumina in the gibbsite alumina series; the use of this metastable phase as a catalyst support has been investigated to a much lesser extent, even though it also demonstrates a relatively high specific surface area and thermal stability. Pansanga et al. have demonstrated that the use of a mixed χ-Al_2O_3 + γ-Al_2O_3 support leads to increased Co dispersion at high Co loadings, but this effect could be mostly due to the morphology of the particles and not necessarily to their surfaces structures [28]. The crystal structure as well as crystallite stacking of χ-Al_2O_3 still remain an open question with several equally feasible viewpoints (see for instance a recent mini-review by Prins [29]). Nevertheless, regardless of the preferred theory on the structure of bulk γ-Al_2O_3 and χ-Al_2O_3, an important difference between these alumina phases lies in the different crystal faces that dominate the surface of the particles.[30,31] As a result, χ-Al_2O_3 differs from γ-Al_2O_3 by the type and density of defect surface sites [32] and by having a higher surface density of weak Lewis acid sites.[33,34] These differences have been suggested to explain different metal sintering behavior.[35] Regarding specifically Co, the presence of χ-phase in γ-Al_2O_3 resulted in higher dispersion of Co as well as higher CO hydrogenation activities of the Co/Al_2O_3 catalysts compared to pure Co/γ-Al_2O_3 samples. In samples of high Co loadings, the spherical-shape-like morphology of the χ-phase Al_2O_3 provides a better stability of the Co particles.[36]

This brief summary of the literature concerning Co nanoparticles on γ-Al_2O_3 and χ-Al_2O_3 reveals the importance of the nanoparticle-support interactions[8,17] that result from an interplay between the support surface structure and its morphology. Here, we show that HRTEM and ^{59}Co IF NMR reveal significant structural differences between the Co NPs supported on γ-Al_2O_3 and χ-Al_2O_3. Finally, building on indirect DFT calculations, we link these differences to the differences in initial distribution of Co precursors on the catalyst surface.

2 Experimental

2.1 Synthesis of Co/γ-Al_2O_3 and Co/χ-Al_2O_3 supported samples

Low-temperature metastable alumina phases were used as the supports for the studied samples. γ-Al_2O_3 was obtained by calcination of pseudoboehmite (Pural SB1, Condea Chemie, Hamburg, Germany) in air at 923 K for 6 h (1.5 K/min heating rate). The same procedure was used to obtain χ-Al_2O_3 from gibbsite (Sigma-Aldrich, Merck, Darmstadt, Germany). XRD and ^{27}Al solid-state NMR techniques (see Supplementary Materials) were used to confirm the purity of the obtained powders as in our previous works [37,38]. The resulting BET (Brunauer-Emmett-Teller) specific surface areas of γ-Al_2O_3 and χ-Al_2O_3 were roughly 175 m^2/g and 150 m^2/g respectively.

In order to determine the moisture capacity of the obtained supports, they were dried at a temperature of 383 K overnight. Then, droplets of distilled water were added to 1 g of alumina under continuous stirring until the sample appeared uniformly wet. The resulting values of moisture capacity were 0.91 ml/g for γ-Al_2O_3 and 0.50 ml/g for χ-Al_2O_3.

Co/Al_2O_3 supported samples with different metallic Co content were obtained using incipient wetness impregnation with an aqueous solution of $Co(NO_3)_2 \cdot 6H_2O$ (98%, Sigma-Aldrich). The higher moisture capacity of γ-Al_2O_3 allowed introducing up to 10 wt.% of Co into the sample with a single impregnation, while χ-Al_2O_3 was able to take only up to 5 wt.% Co in a single impregnation step. Thus, to obtain comparable samples with similar impregnation protocols (meaning having the same Co content obtained by following identical impregnation protocols), 5 wt.% was finally chosen as the target Co content that could be obtained for both supports in a single impregnation step. The samples were impregnated with the Co nitrate solution, then dried at 383 K for 4 hours and calcined in an Ar flow at 623 K for 4 hours. Finally, the samples were reduced in a H_2 stream (50 ml/min) at 673 K for 4 hours (3 K/min ramping rate), purged with Ar for 20 min and sealed in airtight glass ampoules to avoid oxidation. The resulting samples were denoted as 5% Co/(γ-Al_2O_3 or χ-Al_2O_3).

2.2 Characterization techniques

The morphology of the Co nanoparticles was controlled using high-resolution transmission electron microscopy (HRTEM) experiments conducted on a JEM-2010 electron microscope (Jeol, Japan) with acceleration voltage of 200 kV and 0.194 nm spatial resolution. High-angle annular dark field scanning transmission electron microscopy (HAADF-STEM) and elemental mapping images were recorded with 200 kV acceleration voltage using a JEM-2200FS electron

microscope (Jeol, Japan) equipped with a Cs corrector. Particle sizes were analyzed using FIJI software.

^{59}Co internal field NMR (^{59}Co IF NMR) spectra were recorded at 30 K on an AVANCE III 500 Fourier NMR spectrometer (Bruker, USA) using a laboratory-made solid-state probe designed for low-temperature (liquid helium cooling) IF NMR experiments. The probe was operated outside the magnet since IF NMR does not require an external static field. A solid-echo pulse sequence θ-τ-θ was used, with a θ pulse length of 1 μs and an interpulse delay τ of 8 μs. Due to the intrinsically short T_1 nuclear spin relaxation time in ferromagnetic materials, a 33 ms delay between the echo sequences was used. In order to cover the entire frequency range, the spectra were recorded stepwise with 500 kHz carrier frequency steps. A custom automatic tuning and matching device was used to retain a constant quality factor over the entire recording range. In order to determine the intensity of the spectrum at a chosen frequency, the echo signal recorded at this frequency was Fourier-transformed with adequate phase and baseline corrections such that a purely absorption spectrum was obtained. Then, the obtained signal was integrated over a roughly 400 kHz frequency range centered at the carrier frequency, after which the value of the integral was assigned as the intensity of the spectrum at said frequency. Radiofrequency irradiation power was varied at each frequency step to be able to account for the differences of enhancement factors between the bulk of the magnetic domains and the domain walls according to the method originally described by Panissod et al. [39]

^{1}H NMR spectra of the alumina supports were recorded at room temperature using a pulsed NMR spectrometer Bruker Avance 400 with a constant magnetic field of 9.4 T (400.13 MHz ^{1}H Larmor frequency). Prior to the ^{1}H NMR experiments, the samples were dehydrated for 4 hours at 450 °C and sealed inside glass ampoules to avoid rehydration from air. The samples were transferred into standard 4 mm ZrO_2 rotors under argon atmosphere right before the experiment. The spectra were recorded under magic angle spinning condition (MAS, 10 kHz rotation frequency) using a single π/2 pulse (5 μs pulse length). 1024 scans were accumulated with a 5 second delay. Tetramethylsilane was used as an external reference with a chemical shift of 0 ppm.

2.3 Theoretical calculation details

To characterize the hydroxyl coverage of the alumina surfaces, we have conducted DFT calculations of ^{1}H NMR chemical shifts of hydroxyl groups on the two most prominent crystal planes dominating the surfaces of γ-Al_2O_3 (the (110) plane) and χ-Al_2O_3 (the (111) plane) according to the cubic spinel model of the metastable alumina building blocks.

All calculations were performed using the CASTEP program.[40] The interactions between the core ions and the valence electrons were described using the projector augmented wave (PAW) pseudopotentials.[41] The geometry calculations were performed at Γ point with the exchange-correlation functional PW91.[42] A plane wave basis set cut-off energy of 450 eV with the self-consistent field threshold of 10^{-6} eV was used. The geometry calculations used the BFGS (Broyden–Fletcher–Goldfarb–Shanno) algorithm.[43]

To mimic a flat alumina surface, a layer of alumina was created from the spinel structure with the lattice parameter *a* of 8.08534 Å. A model bulk crystal cell was cleaved along the (110) and the (111) crystallographic planes. The (110) cell dimensions were 22.8688×16.1706 Å, while the (111) cell was 19.8048×11.4344 Å. The slab thickness was varied from cell to cell, from 3.5 to 8 Å, with vacuum spans of more than 10 Å to prevent periodic interaction. No additional restrictions were imposed during the structural relaxation. Extra hydroxyl groups were added to the surface Al sites in order to avoid dangling bonds and maintain electroneutrality.

The ^{1}H NMR parameters were computed by the GIPAW method [44] with cutoff energy of 600 eV and PBE (Perdew-Burke-Ernzerhof) functional.[45] The ultrasoft pseudopotentials are the ones supplied with CASTEP.[46].

3 Results

3.1 High-resolution transmission electron microscopy and EDS

Figure 1 (**a, b**) displays typical HRTEM images of the sample 5% Co/γ-Al_2O_3 at different magnifications. According to the micrographs, the γ-Al_2O_3 support consists of large (1 μm) agglomerates of randomly oriented alumina nanocrystallites that are slightly elongated along the [100] axis. Cobalt nanoparticles (shown with white arrows in Fig. 1**b**) are poorly distinguished on the micrographs due to their relatively small size (5.5 nm mean diameter according to HRTEM image analysis). Several Bragg diffraction spots, corresponding to metallic Co crystallites, are clearly visible on the Fourier transform of Fig. 1**b** (Fig. 1**c**) along with the annular diffractions from the randomly oriented crystallites of γ-Al_2O_3. Interplanar distances in *fcc* and *hcp* Co are quite close, which makes the distinction between these crystal structures almost impossible here despite the presence of clearly defined diffraction spots.

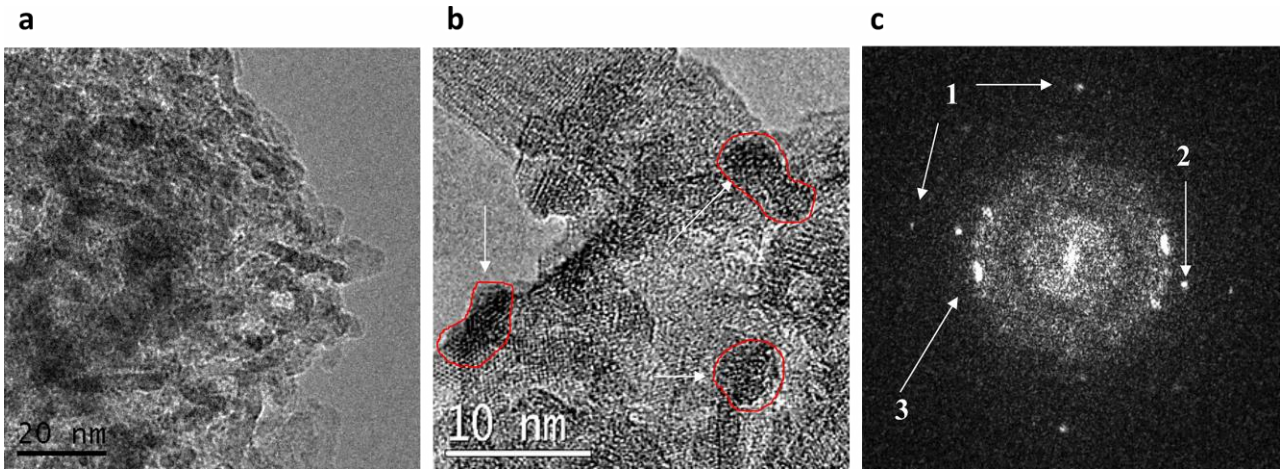

Fig. 1. (**a)** and (**b)**: HRTEM images of the 5% Co/γ-Al_2O_3 sample at different magnifications. Metallic Co nanoparticles are visible as dense dark areas (additionally highlighted with white arrows on b). (**c**): spatial Fourier transform of b). Diffraction spots shown with arrows 1 and 2 correspond to cobalt nanoparticles while the annular diffractions from γ-Al_2O_3 are shown with arrow 3.

A better visualization of distribution of Co nanoparticles on the surface of the support can be obtained from the energy-dispersive mapping images recorded using the HAADF-STEM technique (Fig. 2). In the corresponding EDS maps, areas where the Co $K_{\alpha 1}$ line (6.930 keV) emerges from the background noise are figured in red, while those where the Al $K_{\alpha 1/2}$ line (1.486 keV) emerges are in blue. Thus, at the spatial resolution of the HAADF-STEM image (about 1 nm), Co appeared evenly distributed on the surface of the support and no Co particles could be evidenced by this method.

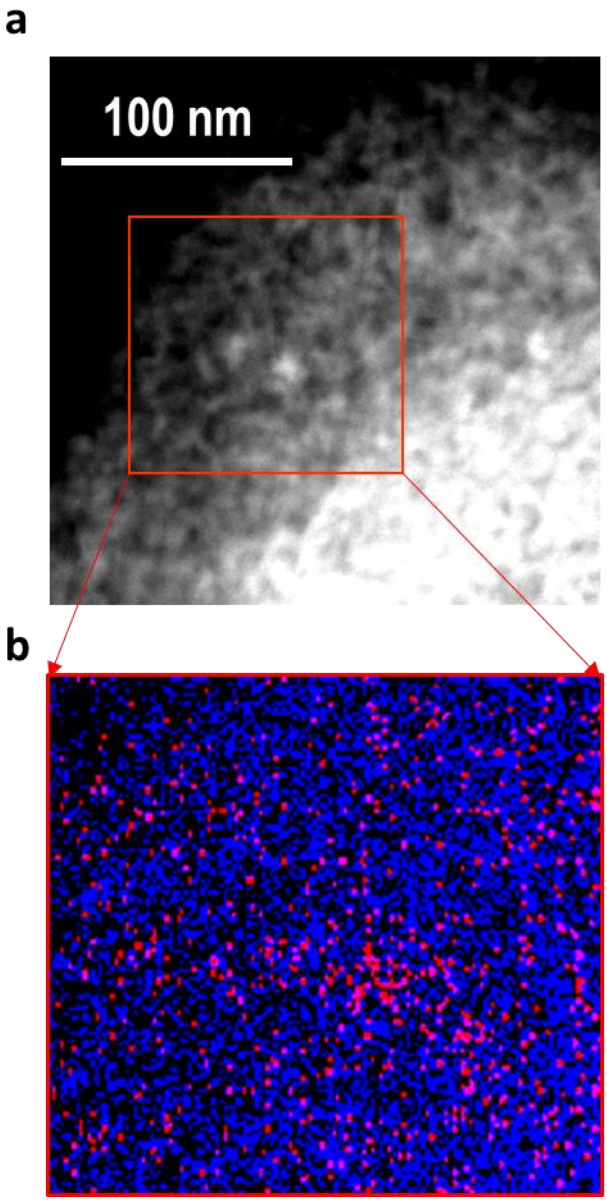

Fig. 2. HAADF-STEM image of the 5% Co/γ-Al_2O_3 sample (**a**) and the elemental mapping of the area in the red box obtained with EDS (**b**). Al signals are shown in blue, Co signals are shown in red.

A significantly different picture can be seen on the HRTEM micrographs of the 5% Co/χ-Al_2O_3 sample (Fig. 3). In this case, the χ-Al_2O_3 support consists of large 0.5 μm platelets (a clear example can be seen in the HRTEM image at low magnification, Fig.S1 in Supplementary Materials). The platelets are built from nanocrystalline domains (about 10x10 nm^2) oriented in the same direction and separated by 3-5 nm-sized pores. On this support, dark areas reveal Co nanocrystallites with sizes of about 5-10 nm. Moreover, EDS images (Fig. 4b) demonstrate that Co was not evenly distributed on the surface of the support. Areas, of sizes up to 100 nm, with higher Co density are visible and coincide with the brighter areas in the HAADF-STEM images

of Figure 4a. Combining these observations leads to the conclusion that Co forms assemblies of ~100 nm consisting of ~10 Co nanocrystallites with sizes of about 5-10 nm each. In addition, the spatial Fourier transform image of the micrograph containing the cobalt nanoparticles (Fig. 3**d**) clearly demonstrates a near overlap of the diffraction spots corresponding to the interplanar distances of the support and of the metallic Co. In this FFT image the diffraction spot of Co metal (d = 0.191 nm, $P6_3/mmc$ space group, PDF №050727) is very close to the brighter diffraction spot that corresponds to χ-Al_2O_3 (d = 0.212 nm). Together with a moiré pattern visible in the supported Co nanoparticles (Fig. 3**c**), this signs an orientation coincidence of the Co nanocrystallite with the alumina crystal domains forming the support surface. This means that both the orientation of growth and the interplanar distance value coincide; suggesting an epitaxial relation between the Co particles and the χ-Al_2O_3 surface.

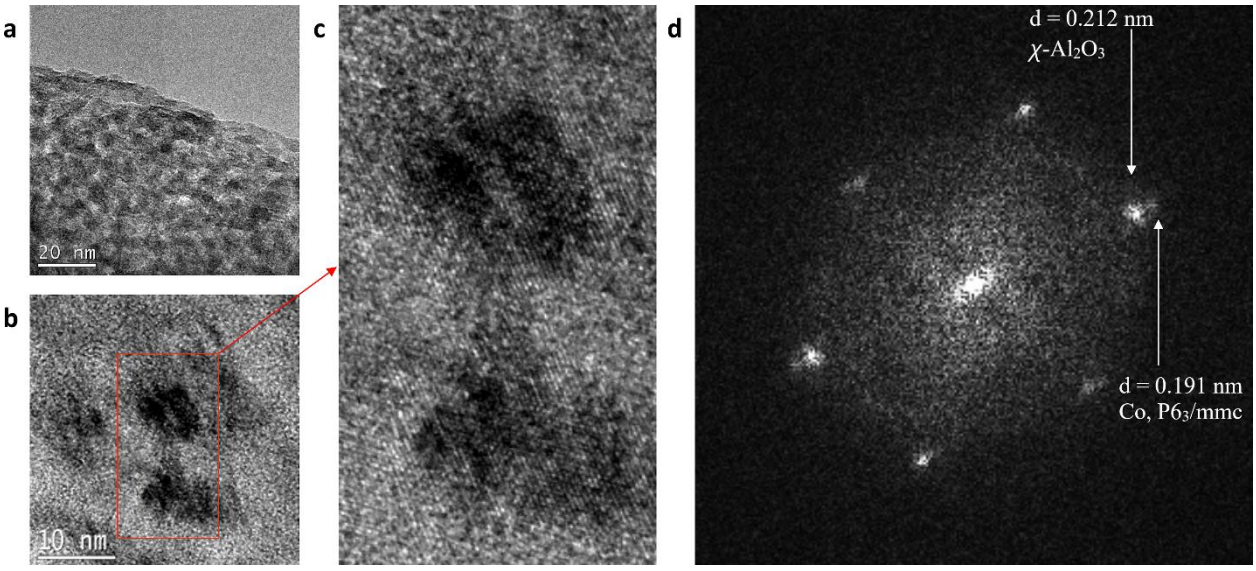

Fig. 3. (**a)** and (**b)**: HRTEM images of the 5% Co/χ-Al_2O_3 sample at different magnifications. Metallic Co nanoparticles are visible as dense dark areas. **(c):** Magnification of the area inside the red box of b). **(d):** Spatial Fourier transform of b). The diffraction spots corresponding to the Co metal and χ-Al_2O_3 are denoted with white arrows. Such a close arrangement of diffraction spots in distance and angle suggests epitaxy between the Co nanoparticle and the surface of the support.

Thus, HRTEM and HAADF-STEM techniques demonstrate that, at 5% Co loading, the χ-Al_2O_3 surface appeared much more ordered than the one of γ-Al_2O_3 and that the Co nanoparticles were oriented in epitaxial relation with the χ-Al_2O_3 surface. Additionally, elemental mapping

images show that cobalt was more homogeneously dispersed over the surface of γ-Al_2O_3 in the form of small (5 nm and less) nanocrystallites, while larger Co nanocrystallites (5-10 nm) tended to associate on the surface of χ-Al_2O_3.

Electron microscopy techniques revealed the morphology and structure of the samples, but due to their strictly local character, these methods are not optimal for studying the crystal structure of Co nanoparticles in the entire volume of the sample. On the other hand, ^{59}Co internal field NMR (^{59}Co IF NMR) is a technique able to discern between different types of crystal structure of metallic Co in the bulk – something that is more likely to relate to the overall efficiency of the catalyst.

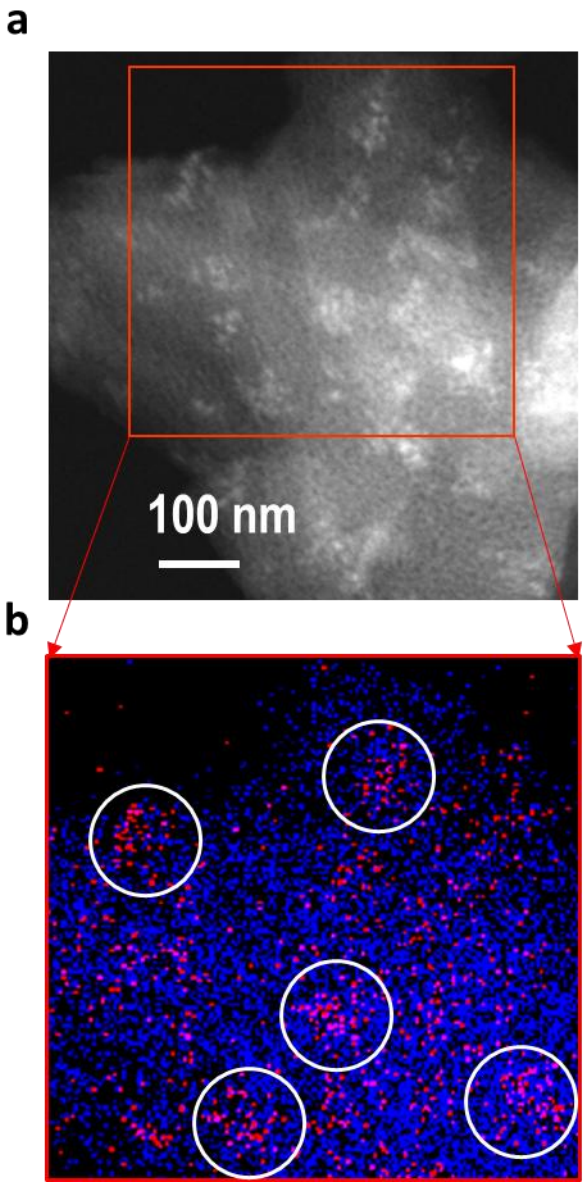

Fig. 4. HAADF-STEM image of the 5% Co/χ-Al_2O_3 sample (**a**) and the elemental mapping of the area in the red box obtained with EDS (**b**), Al signals are shown in blue, Co signals are shown in red. White circles in (b) are used to locate the large Co NP assemblies identified as brighter areas in (a). Individual points on the EDS elemental maps do not indicate the presence of Co with certainty because their appearance may be connected with the background noise in the EDX spectra. However, since noise is expected to be randomly distributed on the elemental maps, the areas that contain larger densities of points (shown with the white circles in Fig. 4b) can be associated with Co particles and do indeed coincide with the brighter areas of the HAADF-STEM image (Fig. 4a).

3.2 ^{59}Co internal field nuclear magnetic resonance

^{59}Co IF NMR spectra reflect both the crystal and the magnetic structures of Co nanoparticles, which affect the hyperfine magnetic field at the location of the nucleus. It can be observed only in ferromagnetic particles. In superparamagnetic ones, the internal field fluctuates rapidly at the timescale of the NMR experiments and no signal is generated. Consequently, we have demonstrated earlier that the size of Co nanoparticles is an equally important factor affecting the ^{59}Co IF NMR spectra when particles below the nominal critical superparamagnetic size are present in the sample and invisible in the IF NMR spectra. The critical size below which particles isolated from each other are superparamagnetic (and thus are undetectable in IF NMR) at room temperature was shown to be equal to roughly 7.5 nm in diameter for isolated particles.[21] However, in non-isolated particles, magnetic ordering of the particles due to interparticle magnetic interactions (dipolar and exchange) affects the critical size for superparamagnetic/ferromagnetic transition in a way that is difficult to predict quantitatively. In practice, we can consider the particles to be isolated when the energy of dipolar interaction between the particles is much smaller compared to magnetic anisotropy energy[47], which is the case for Co particles about 5 nm in diameter and separated by at least the same distance. Considering this, and according to the electron microscopy data, a significant fraction of Co nanoparticles in the 5% Co/γ-Al_2O_3 and 5% Co/χ-Al_2O_3 samples could be superparamagnetic and undetectable by ^{59}Co IF NMR at room temperature. Therefore, we conducted the ^{59}Co IF NMR experiments at 30 K where the critical particle size for superparamagnetic transition decreases to 3.5 nm. It can then be safely assumed that almost all Co particles in the studied samples are in a ferromagnetic state and contribute to the ^{59}Co IF NMR spectra.

As stated in the experimental section and according to a now well-established procedure,[21] the spectra were recorded at different radiofrequency powers in order to discern between the multi domain and single domain ferromagnetic particles. The distribution of optimal radiofrequency power (power at which the spectral intensity at the chosen frequency is maximum) for all spectra was practically uniform meaning that we have not detected any multi domain Co particles. This is in complete agreement with the observations made using HRTEM since multiple magnetic domains are not expected to occur in particles smaller than 70 nm.[48] Therefore, all of the obtained spectra were analyzed from the standpoint of single domain particles.

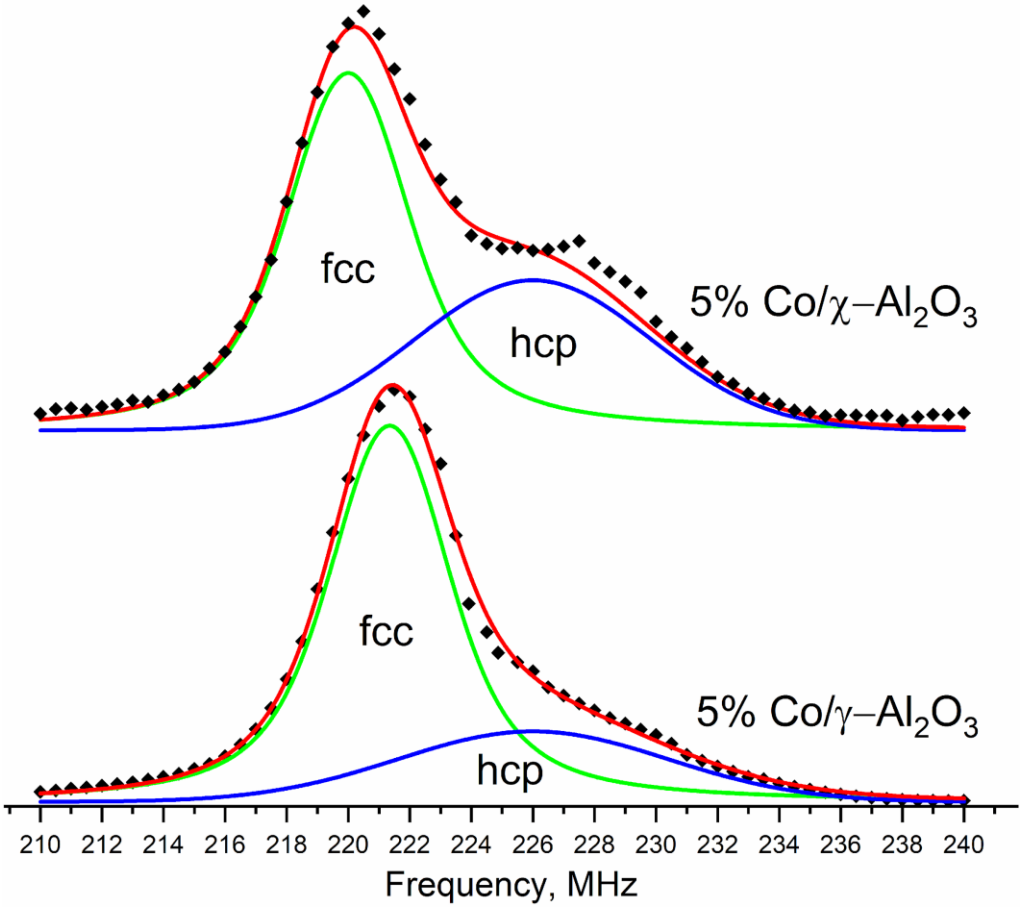

Fig. 5. ^{59}Co IF NMR spectra of the 5% Co/γ-Al_2O_3 (bottom) and 5% Co/χ-Al_2O_3 (top) samples. T = 30 K. Spectra are normalized to the same maximal intensity. Echo measurement points are shown with symbols, while the lines show the result spectral decomposition into two Pseudo-Voigt profiles for *fcc* Co (green) and *hcp* Co (blue). The sum of these two profiles is shown in red.

^{59}Co IF NMR spectra of the studied samples recorded at 30 K are shown in Fig. 5. The spectrum of the sample supported on γ-Al_2O_3 (bottom) displays a dominant line centered at 222 MHz that corresponds to single domain particles with *fcc* structure [26]. The relatively weak wide shoulder stretched from 224 MHz to 235 MHz indicates the minor occurrence of particles with *hcp* structure [26]. The *hcp* crystal structure is the stable form of bulk Co at, and below, room temperature (the *hcp*– *fcc* transition is known to happen at roughly 700 K). However, according to many experimental observations, the decrease of the size of Co nanoparticles leads to the stabilization of the *fcc* crystal phase to the extent that this phase becomes dominant for relatively small nanoparticles, as observed here.[49,50] Thus, the obtained spectrum further corroborates the electron microscopy observation that Co was present as highly dispersed small

nanoparticles over the surface of the support in the case of γ-Al_2O_3. Tsakoumis et al. have shown using HRTEM that even at a 20 wt.% Co loading, Co nanoparticles supported on the surface of γ-Al_2O_3 have an average size of 5.2 nm with no particles larger than 14 nm in diameter.[8] This is consistent with the observed prevalence of the *fcc* Co signal in the ^{59}Co IF NMR spectrum of the sample supported on γ-Al_2O_3 reported here.

In the spectrum of the 5% Co/χ-Al_2O_3 sample (Fig 5, top), one can observe a similar line shape consisting of two broad signals corresponding to single domain *fcc* and *hcp* phases of Co, with the *fcc* line undergoing a 1 MHz frequency shift compared to the 5% Co/γ-Al_2O_3 sample. The quantitative analysis of the *fcc* and *hcp* fractions in the samples can be made by decomposition of the experimental spectra into two broad peaks. The signal from the *fcc* and *hcp* packed Co can be represented as two Pseudo-Voigt profiles centered around 220 MHz and 227 MHz respectively, with the line for *hcp* Co being much broader than the line of *fcc* Co due to stronger magnetic anisotropy in the former case [51]. The end results of such decomposition (shown as colored lines in Fig. 5), namely the relative intensities of the *fcc* and *hcp* signals, reflect the relative contents of these crystal phases in the samples, which were 24% of *hcp* Co for γ-Al_2O_3 and 39% *hcp* Co for χ-Al_2O_3. These values constitute a lower estimate. Indeed, very small *fcc* Co particles being superparamagnetic might not contribute to the IF NMR spectra.

3.3 Experimental and predicted ^{1}H chemical shifts

The initial stage in the formation of Co nanoparticles on the surface of the support is the anchoring of Co(II), from the precursor ions, onto the available vacant sites. Using EXAFS and *ab initio* calculations of the adsorption energy of Co on different surfaces of α-Al_2O_3, Chizallet et al. [52] have recently demonstrated that the hydroxyl coverage of the surface and the location of the surface vacancies greatly influence the interaction energy of Co(II) with the alumina surface.

Determining *ab initio* the hydroxyls on the alumina surface susceptible of interacting with different amounts of Co(II) is obviously very informative but requires lengthy computations involving large sets of models with different types of alumina surfaces together with the necessary water to coordinate and stabilize the dangling groups. We tried instead a semi empirical approach based on correlating the experimentally observed and theoretically predicted ^{1}H NMR shifts.

In order to do so, the first step is to choose a reliable structural model of γ-Al_2O_3 and χ-Al_2O_3 surfaces. While modeling the surface of the stable trigonal α-alumina is relatively straightforward due to its completely refined crystal structure, the structures of metastable alumina remain disputed. The low temperature γ-Al_2O_3 metastable phase, in particular, has attracted the highest attention due to its relevance as an heterogeneous catalyst and catalyst support. γ-Al_2O_3 is generally considered to have a cubic spinel structure [29,53], even though the stoichiometry of Al_2O_3 does not directly correspond to a spinel AB_2O_4. Such structural disparity has led to different models describing the distribution of Al ions and vacancies in the spinel cationic sublattice [29]. Despite the differences of these models, the majority of researchers agree that the bulk structure of γ-Al_2O_3 particles belongs to the cubic spinel type. However, the surface structures and bonding scheme of these particles remain debated; therefore a brief discussion of existing models is necessary before proceeding further.

The most widely used model of metastable alumina surfaces was proposed by Knözinger and Ratnasamy [54]. It consists of bulk spinel structure cleavages along (100), (110) and (111) crystal planes. The reactivity of such surfaces in hydrated conditions mainly depends on the hydroxyl coverage obtained by addition of protons and hydroxyls to compensate for the charge and complete the coordination symmetry of surface Al and O sites [55,56]. Further improvements of this model include reconsiderations of the bulk alumina structure to non-spinel models [57], as well as accounting for the finite size effect [58,59] and for stacking faults of individual alumina crystallites [30].

The first consequence of the finite size of an alumina crystallite is the presence of edges between its surfaces, which leads to the occurrence of unique hydroxyl sites that are not hydrogen-bonded to other hydroxyl groups and remain highly reactive to chlorination, as was shown by ^{1}H NMR and *ab initio* calculations by Batista et al. [58]. The second important effect of the finite particle size is linked to the synthetic routes used to obtain the metastable aluminas. Most frequently, aluminum oxides are obtained through dehydration of corresponding hydrates, as was experimentally demonstrated by Stumpf et al [60]. In this case, the restructuring of individual particles is governed by topotactic transformations during which the structural features of the initial particles are conserved. Due to the layered nature of the alumina hydrates, the topotactic transitions result in differences between alumina surfaces that formally belong to the same crystal plane family (e. g. (110) cubic spinel plane) depending on basal/lateral position in the initial particle, as was demonstrated using DFT calculations in the recent paper by Pigeon et al. [59].

Additionally, metastable aluminas are intrinsically nanostructured materials, thus the description of their structures requires to account for the defectiveness and stacking of the individual crystallites that also play an important role on the formation of the particle surfaces. The approach developed by Tsybulya et al. accounts for the connectivity of individual spinel crystallites through planar defects lying in the (100), (110) and (111) crystal planes of cubic spinel [30]. This technique allowed modeling the structures of low-temperature aluminas as well as demonstrating the effect of abundant shearing planar defects that allow the existence of a cubic spinel material with a non-spinel stoichiometry. Later, this approach was also used by Pakharukova et al. to create 3D nanostructured models of γ-Al_2O_3 particles and simulate the XRD patterns, which coincide with experimental XRD patterns and allow to explain the diffuse nature of several peaks [61].

Both the topotactic transition and crystallite stacking approaches do not contradict each other, but provide a complementary description of both the bulk and the surface of metastable alumina nanoparticles. Importantly, both of these approaches coincide in their prediction of the crystal planes that form the surface of γ-Al_2O_3 nanoparticles, namely (100) and (110) crystal planes with the minor presence of the (111) plane.

The much less investigated structure of the metastable χ-Al_2O_3 obtained through dehydration of aluminum trihydroxide gibbsite remains an open question without any commonly accepted viewpoint. The source of this controversy lies in the presence of a diffuse scattering peak at $2\theta = 43°$ in its XRD pattern that does not belong to the cubic spinel structure, even though the rest of the XRD pattern corresponds to the said structure. Additionally, the ^{27}Al NMR

spectra reveal an $Al^{[6]}$:$Al^{[4]}$ equal to roughly 3:1 that does not correspond to the spinel structure for which this ratio is expected to be 2:1 (as observed in ^{27}Al NMR spectra of γ-Al_2O_3) [62]. However, recently, Yatsenko et al. [63] have shown using the "crystallite stacking" approach that the non-spinel diffuse scattering peak of χ-Al_2O_3 may appear due to planar defects of the anion sublattice of cubic spinel structure (the O^{2-} sublattice in ratioAB_2O_4 spinel follows a regular *fcc* pattern, while such planar defects change its local ordering to *hcp*). This observation allows one to consider the particles of χ-Al_2O_3 as having the cubic spinel structure when trying to model its surface in the same way as it was done for γ-Al_2O_3. Considering this, the surface of χ-Al_2O_3 is mostly represented by the (111) spinel crystal plane, as was shown in [30]. Moreover, if we apply the same logic of topotactic transitions to the well-refined structure of gibbsite just as it was done for boehmite in the case of γ-Al_2O_3, the result for the most exposed crystal plane will be the same. Indeed, the hexagonally symmetric particles of gibbsite have a layered structure, with the layers of aluminum octahedral separated by hydrogen-bonded hydroxyl layers in the direction perpendicular to the [001] axis. Thus, the (001) crystal plane that has a hexagonal symmetry is the most prevalent for the gibbsite particles [64,65]. According to Mitsui et al. [66], gibbsite particles retain their morphology during the dehydration into χ-Al_2O_3 including the hexagonal symmetry of the (001) basal planes. Therefore, the retention of the particle morphology and the surface prevalence of the hexagonally symmetric planes (001) in the case of gibbsite and (111) in the case of χ-Al_2O_3 allow us to assume that the (001) basal planes of gibbsite undergo a transition into the (111) planes of the dehydrated alumina.

In summary, the surface of metastable aluminas can be accurately described in terms of spinel crystal planes, mainly (100) and (110) with the minor presence of the (111) for γ-Al_2O_3 nanoparticles, and (111) for χ-Al_2O_3.

Consequently, the γ- and χ-Al_2O_3 surfaces (Fig. 6) were modeled by cleaving the crystal structure along the directions of the (110) of (111) crystal planes. We also note that such a representation of the particle surface as an infinite slab cannot possibly account for the edges formed between the crystallite surfaces or for the subtle features of the crystal planes formed during the topotactic transition. Nevertheless, such an approach can still be feasible and useful for the prediction of the general behavior of the alumina surface towards the hydrated Co ions in the precursor solution. By using the similar infinite slab model, Larmier et al. [17] have demonstrated the so-called structural recognition of Co^{2+} ions on the (100) and (110) surfaces of a cubic spinel model of γ-Al_2O_3. They have shown that the most energetically favorable mode of adsorption of Co^{2+} ions is the one during which octahedral complexes including one or two bonds between Co^{2+} and lattice oxygen are formed.

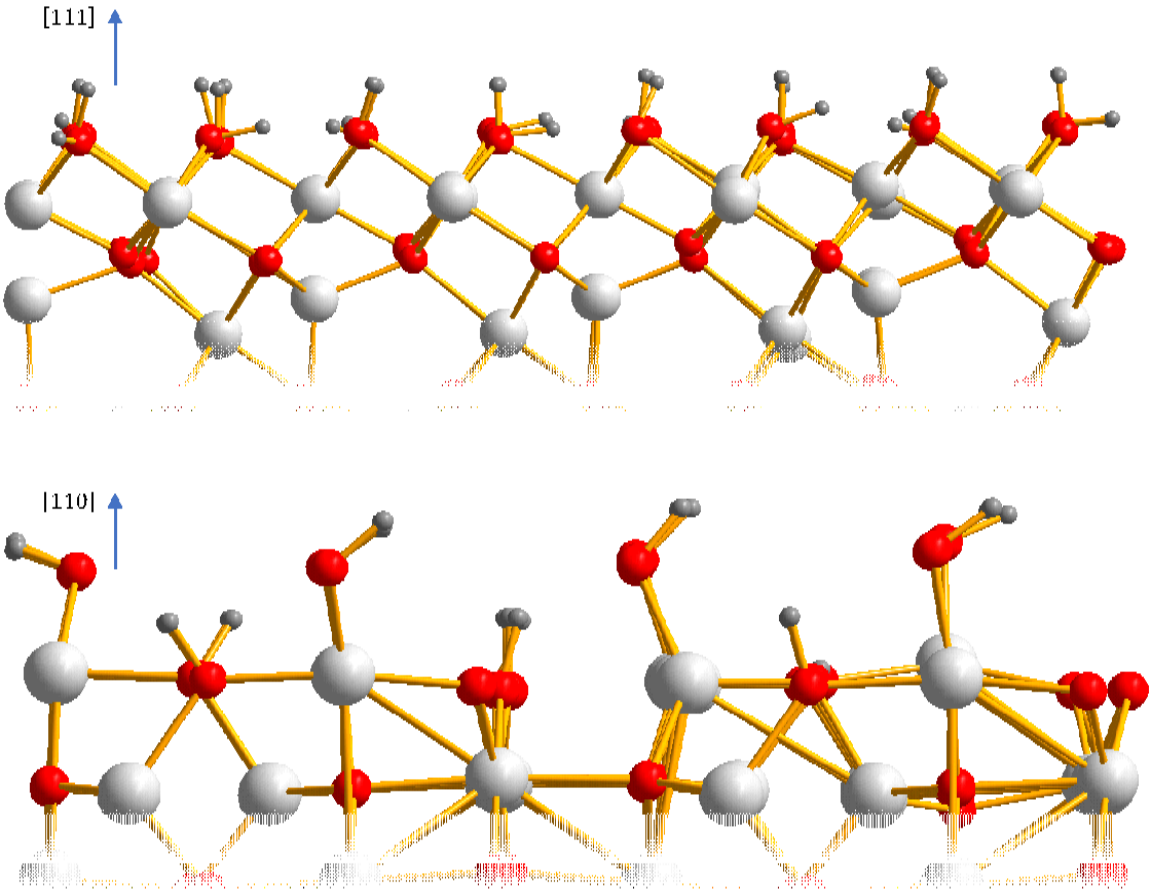

Fig. 6. Models of the (111) (top) and (110) (bottom) crystal planes of the spinel structure of crystallites forming metastable alumina phases. Al atoms are shown in silver, O atoms are shown in red, H atoms are shown in black. Green circles and lines denote the positions of the Al atoms that are missing from the next layer. Such sites can form vacancies available to Co^{2+} ions.

The hydroxyl groups were added to the spinel slabs to compensate for the charge and any dangling bonds that were formed during the cleavage (more details can be found in the Experimental section). After the relaxation of the structures without any additional constraints, we calculated the ^{1}H chemical shifts of all the hydroxyl groups now present on these model surfaces. The resulting sets of calculated chemical shifts ascribed to the (110) and (111) surfaces, as well as their comparison with the experimental ^{1}H NMR spectra, can be found in Fig. 7 (calculated spectra are shown with colored lines, while the experimental data are shown in black). Both the calculated sets of chemical shifts and the experimental ^{1}H 10 kHz MAS NMR spectra displayed a significant difference in the spectral intensity in the 5-10 ppm region. Namely, the intensity in this region was zero for the (111) plane model, which agreed well with the low relative intensity observed in the same region of the experimental spectrum of χ-Al_2O_3. Furthermore, edges between the spinel surfaces are present in both samples, resulting in

additional terminal hydroxyl groups that give rise to a distinct line at 0 ppm in the experimental spectra (blue line in Fig. 7**a, b**), as was predicted by Batista et al. [58]. These hydroxyl groups were obviously missing from the perfect plane models and thus, had to be added to the decomposition of the experimental spectra manually. The experimental spectra were decomposed into the theoretical spectra for (111) and (110) planes as well as the line corresponding to surface edges until the best match was achieved. The resulting relative intensities of the theoretical spectra of crystal planes excluding the surface edges were: 50% (111) plane and 50% (110) plane for χ-Al_2O_3; 30% (111) plane and 70% (110) plane for γ-Al_2O_3. Thus, the ^{1}H NMR data demonstrate that the surface of γ-Al_2O_3 is mostly represented by the (110) crystal plane, while an equal mixture of (111) and (110) spinel crystal planes makes up the surface of χ-Al_2O_3. The difference between the compositions of these surfaces can play an important role during their interaction with the Co impregnation solution since hydroxyl coverages of the spinel crystal planes differ significantly: the hydration of the (111) spinel plane gives rise exclusively to bridging (μ_2- and μ_3-OH) groups, while the (110) spinel plane contains a mixture of terminal (μ_1-OH) and bridging (μ_2-OH) groups.

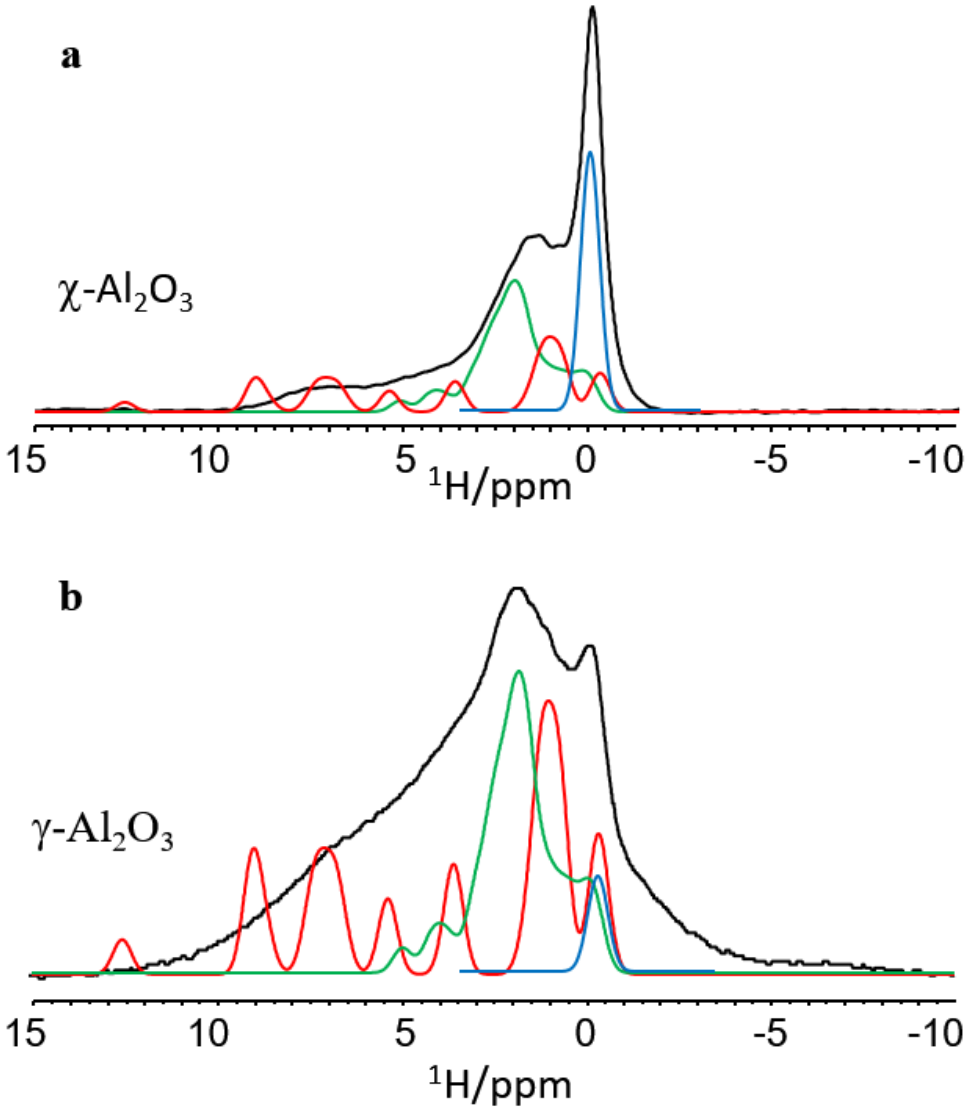

Fig. 7. Decomposition of the experimental 10 kHz MAS ^{1}H NMR spectra of dehydrated |-Al_2O_3 (**a**, black line) and ©-Al_2O_3 (**b**, black line) into the theoretically calculated spectra for (110) and (111) spinel planes (red and green lines, respectively) and the separate line corresponding to hydroxyl groups supported on the edges between the crystallite surfaces according to ref. [58] (blue line). The relative contributions of the (111) and (110) planes to the spectra, excluding the signal at 0 ppm, were: 50% (111) plane and 50% (110) plane in the case of χ-Al_2O_3; 30% (111) plane and 70% (110) plane in the case of γ-Al_2O_3. Note, that the given values reflect the surface densities of the OH groups and correspond directly to the surface areas represented by these planes in the samples.

4 Discussion

Larmier et al. have shown, using DFT calculations, that epitaxial interaction of aqueous cobalt precursor with the surface of γ-Al_2O_3 (modeled as (100) and (110) infinite cleaved slabs) is energetically favorable during the impregnation and drying stages of FTS catalyst synthesis.[17] This interaction was linked to the formation of the mixed cobalt-aluminum oxide layer at the interface between the support surface and Co nanoparticle through structural recognition. Simply put, Co^{2+} ions from the impregnation solution tend to occupy the vacancies created by removal of the octahedral Al^{3+} sites, which leads to the creation of stable octahedral Co^{2+} complexes and dispersion of Co over the surface of the support. This, in turn, may lead to the deactivation of small (less than 5.3 nm in diameter) Co nanoparticles during the onset of FTS or to a complete inactivity of the sample in the extreme case of very small (less than 3 wt.%) Co loading [8].

The epitaxial relation between the reduced Co nanoparticles and the surface of χ-Al_2O_3 that we observed by HRTEM in the reduced sample was necessarily a direct consequence of a strong particle-support interaction at some stage of the synthesis. However, the effects of this interaction were strikingly different in the cases of γ- and χ-Al_2O_3. The key differences between these supports lie firstly in the crystal planes dominating their surface and secondly in the morphology of the particles.

As apparent from our semi empirical modeling of alumina surfaces, γ- and χ-Al_2O_3 differ by the nature of crystal planes at their surface thus leading to completely different types of hydroxyl coverage. The hydroxyl coverage of (111) plane (and correspondingly χ-Al_2O_3, Fig. 6 top) consists exclusively of bridging hydroxyl groups located under the potential vacancies (missing Al^{3+} sites, shown with green circles in Fig. 6, top), thus preventing them from stabilizing any adsorbed ion. For the (110) plane (dominating the surface of γ-Al_2O_3, Fig. 6 bottom) we observe a picture strongly resembling the C-μ_1-μ_2 model presented by Chizallet et al. [52], with the main similarity being the mixed terminal-bridging hydroxyl coverage. This, in turn, is connected with the presence of a plane below the level of terminal hydroxyl where vacancies for octahedral complexes can form and provide direct anchoring to the lattice O^{2-} (Fig. 6, bottom). According to DFT calculations made by Chizallet et al., these vacancies provide a large gain in the absorption energy during the onset of $Co(OH)_2$ formation. Such increased strength of interaction between the metallic Co precursor and the surface of the support would inevitably lead to strong dispersion of Co^{2+} ions over the surface of γ-All_2O_3 that would, in turn, result in a large amount of hard-to-reduce Co species and a decrease of the metallic Co particle

size. A prominent signal at 0 ppm in the ^{1}H NMR spectrum of χ-Al_2O_3 is also worth noting because, according to work by Batista [58], this chemical shift range corresponds to the hydroxyl groups supported on the edge between the crystallite surfaces of the particle. Even though the relative content of these hydroxyl groups is high, they do not facilitate the anchoring of the Co^{2+} ions due to their location. Indeed, the edges contain undercoordinated sites and cannot provide a suitable vacancy for an octahedral Co^{2+} complex.

Thus, the modeling of the hydroxyl coverage helps rationalize the observations made using HRTEM and ^{59}Co IF NMR; namely, the smaller particle size and the prevalence of *fcc* metallic Co in the sample supported on γ-Al_2O_3 after calcination and reduction, when compared to the sample supported on χ-Al_2O_3. The same rationalization may also be made for the difference in moisture capacities that we observed during the sample preparation while the specific surface areas of the powders were very close. The role of surface hydroxyl coverage during surface wetting has been studied for many oxide materials including Al_2O_3 [67,68]. Dangling hydroxyl groups available for the formation of H-bonds with the water molecules were shown to facilitate the formation of a liquid water layer on the surface of all of the studied oxides. Thus, the higher moisture capacity of γ-Al_2O_3 can also be ascribed to the presence of terminal hydroxyl groups on (110) plane, representing the majority of its surface.

Furthermore, the remarkable coincidence of the structural parameters of the metallic Co particles and the surface of χ-Al_2O_3 cannot be ignored here. The hexagonally symmetric pattern of its surface could be directly explained by the topotactic transformations of gibbsite particles as mentioned above. This direct observation of the prominent (111) crystal plane in HRTEM images of χ-Al_2O_3 serves as further proof for the spinel-based models of its crystal structure and may shed light on what can be called structural recognition. In the view of the (111) surface model presented in the preceding section (Fig. 8), it can be inferred that the missing Al atoms (possible vacant sites for Co^{2+} anchoring) also follow a hexagonal pattern. Moreover, the morphology of χ-Al_2O_3 particles that includes relatively large and oriented crystallites would favor the formation of larger and well-ordered metal particles. However, the distance between any two closest "vacancies" (approximately 4.5 Å) is much larger than the Co-Co distance in the metallic cobalt (approximately 2.5 Å). Consequently, we cannot say that this simple vacancy model determines the way in which the Co nanoparticles are formed after reduction. Nevertheless, it is reasonable to assume that the hexagonal symmetry of the surface of χ-Al_2O_3 promotes the *hcp* phase formation which appeared to be favored, as deduced from the experimental NMR observations.

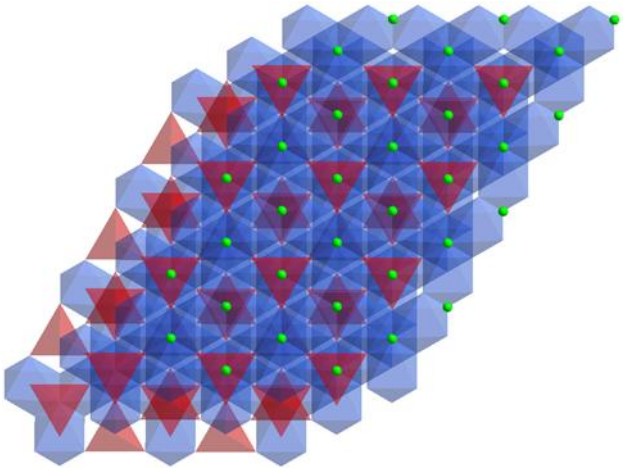

Fig. 8. View on the (111) plane from the above. Tetrahedral Al sites are depicted with red, octahedral Al sites are depicted with blue. Green dots represent the possible vacancies.

5 Conclusions

Rational design of supported cobalt catalysts requires an efficient way to predict the catalytic properties of Co nanoparticles based on their structural and morphological properties. Such predictions were made possible by the extensive studies on the influence of Co NP sizes and crystalline structures on their activity and selectivity. In this work, the application of a non-local technique such as ^{59}Co Internal Field NMR spectroscopy in combination with local electron microscopic techniques proved to be very efficient. It provided an efficient way to investigate the structure and size (partially through the dependence on the stability of different crystal structures on the size of the nanoparticles) of the cobalt nanoparticles on the surface of the sample.

In particular, we have demonstrated that χ-Al_2O_3 makes more favorable the *hcp* structure for supported Co metal nanoparticles, which is related to the presence of larger particles when compared to the ones supported on γ-Al_2O_3, as revealed by 30 K ^{59}Co NMR experiments. Correspondingly, the elemental mapping performed during the STEM experiments revealed the presence of 5-10 nm metallic Co particles assembled into patches on the surface of χ-Al_2O_3 in contrast to highly dispersed Co on the surface of γ-Al_2O_3. Such a difference between these metastable alumina phases could be attributed to the alumina particle morphologies observed in HRTEM micrographs. γ-Al_2O_3 formed aggregates of small randomly oriented nanocrystallites, while the χ-Al_2O_3 sample consisted of larger micron-sized plates oriented in the same crystalline direction that gave rise to a hexagonal pattern of diffraction spots in the Fourier transform analysis. Such particle morphologies, together with the slightly smaller specific surface area of χ-

Al_2O_3, would naturally lead to larger Co particles reduced on this support. Additionally, in agreement with the works by Chizallet et al.[52] and Larmier et al. [17], the hydroxyl coverage of Al_2O_3 plays an important role in the formation of Co particles by creating vacant sites that can accommodate an octahedral Co^{2+} complex anchored directly to the O^{2-} sublattice.

According to the approach developed by Tsybulya, different metastable aluminas consist of similar spinel blocks but stacked in different ways;the crystal planes most prominent on the surface of their particles also differ. This allowed us to create simple models of χ-Al_2O_3 and γ-Al_2O_3 surfaces, and in particular of their hydroxyl coverages. As we confirmed using ^{1}H MAS solid-state NMR and *ab initio* DFT calculations of ^{1}H chemical shifts, the (111) crystal plane representing the surface of χ-Al_2O_3 contained exclusively bridging hydroxyl groups, while the (110) crystal plane prominent in γ-Al_2O_3 contained a mixture of bridging and terminal hydroxyls. According to the literature, the presence of both types of hydroxyl groups facilitates both the wetting of the surface and the dispersion of Co cations over the surface of the support. This, in turn, would facilitate the dispersion of metallic Co apparent in 5% Co/γ-Al_2O_3 sample.

This is in complete agreement with our experimental observations by HRTEM and IF NMR of larger *hcp* Co particles on χ-Al_2O_3. The structure and particle morphology of χ-Al_2O_3 led to the formation of larger Co nanoparticles with higher *hcp* Co content as compared to γ-Al_2O_3. The *hcp* Co structure is further stabilized by the hexagonal symmetry of the (111) spinel crystal plane. Thus, the type of the surface of the alumina support can influence the size and crystal structure of the supported Co nanoparticles, which provides further possibility for deposition of Co nanoparticles with the desired catalytic properties.

6 Acknowledgements

The reported study was funded by RFBR according to the research project No. 20-33-90184. This work was partially supported by the Ministry of Science and Higher Education of the Russian Federation within the governmental order for Boreskov Institute of Catalysis (project AAAA-A21-121011390054-1). NMR equipment at ESPCI Paris is funded in part by the Paris Region. I.V.Y. benefited from the Vernadski PhD fellowship from the French Embassy in Moscow.

7 References

[1] T.W. van Deelen, C. Hernández Mejía, K.P. de Jong, Control of metal-support interactions in heterogeneous catalysts to enhance activity and selectivity, Nat Catal. 2 (2019) 955–970. https://doi.org/10.1038/s41929-019-0364-x.

[2] O. Ducreux, B. Rebours, J. Lynch, M. Roy-Auberger, D. Bazin, Microstructure of Supported Cobalt Fischer-Tropsch Catalysts, Oil & Gas Science and Technology - Revue de l'IFP. 64 (2009) 49–62. https://doi.org/10.2516/ogst:2008039.

[3] D.I. Enache, B. Rebours, M. Roy-Auberger, R. Revel, In Situ XRD Study of the Influence of Thermal Treatment on the Characteristics and the Catalytic Properties of Cobalt-Based Fischer–Tropsch Catalysts, Journal of Catalysis. 205 (2002) 346–353. https://doi.org/10.1006/jcat.2001.3462.

[4] H. Karaca, O. V. Safonova, S. Chambrey, P. Fongarland, P. Roussel, A. Griboval-Constant, M. Lacroix, A.Y. Khodakov, Structure and catalytic performance of Pt-promoted alumina-supported cobalt catalysts under realistic conditions of Fischer–Tropsch synthesis, Journal of Catalysis. 277 (2011) 14–26. https://doi.org/10.1016/j.jcat.2010.10.007.

[5] M.K. Gnanamani, G. Jacobs, W.D. Shafer, B.H. Davis, Fischer–Tropsch synthesis: Activity of metallic phases of cobalt supported on silica, Catalysis Today. 215 (2013) 13–17. https://doi.org/10.1016/j.cattod.2013.03.004.

[6] S. Lyu, L. Wang, J. Zhang, C. Liu, J. Sun, B. Peng, Y. Wang, K.G. Rappé, Y. Zhang, J. Li, L. Nie, Role of Active Phase in Fischer–Tropsch Synthesis: Experimental Evidence of CO Activation over Single-Phase Cobalt Catalysts, ACS Catalysis. 8 (2018) 7787–7798. https://doi.org/10.1021/acscatal.8b00834.

[7] J.-X. Liu, H.-Y. Su, D.-P. Sun, B.-Y. Zhang, W.-X. Li, Crystallographic Dependence of CO Activation on Cobalt Catalysts: HCP versus FCC, Journal of the American Chemical Society. 135 (2013) 16284–16287. https://doi.org/10.1021/ja408521w.

[8] N.E. Tsakoumis, J.C. Walmsley, M. Rønning, W. van Beek, E. Rytter, A. Holmen, Evaluation of Reoxidation Thresholds for γ-Al_2O_3-Supported Cobalt Catalysts under Fischer–Tropsch Synthesis Conditions, Journal of the American Chemical Society. 139 (2017) 3706–3715. https://doi.org/10.1021/jacs.6b11872.

[9] G.L. Bezemer, J.H. Bitter, H.P.C.E. Kuipers, H. Oosterbeek, J.E. Holewijn, X. Xu, F. Kapteijn, A.J. van Dillen, K.P. de Jong, Cobalt Particle Size Effects in the Fischer−Tropsch Reaction Studied with Carbon Nanofiber Supported Catalysts, Journal of the American Chemical Society. 128 (2006) 3956–3964. https://doi.org/10.1021/ja058282w.

[10] A. Barbier, A. Tuel, I. Arcon, A. Kodre, G.A. Martin, Characterization and Catalytic Behavior of Co/SiO_2 Catalysts: Influence of Dispersion in the Fischer–Tropsch Reaction, Journal of Catalysis. 200 (2001) 106–116. https://doi.org/10.1006/jcat.2001.3204.
[11] A. Tuxen, S. Carenco, M. Chintapalli, C.-H. Chuang, C. Escudero, E. Pach, P. Jiang, F. Borondics, B. Beberwyck, A.P. Alivisatos, G. Thornton, W.-F. Pong, J. Guo, R. Perez, F. Besenbacher, M. Salmeron, Size-Dependent Dissociation of Carbon Monoxide on Cobalt Nanoparticles, Journal of the American Chemical Society. 135 (2013) 2273–2278. https://doi.org/10.1021/ja3105889.
[12] E. Rytter, N.E. Tsakoumis, A. Holmen, On the selectivity to higher hydrocarbons in Co-based Fischer–Tropsch synthesis, Catalysis Today. 261 (2016) 3–16. https://doi.org/10.1016/j.cattod.2015.09.020.
[13] N.E. Tsakoumis, M. Rønning, Ø. Borg, E. Rytter, A. Holmen, Deactivation of cobalt based Fischer–Tropsch catalysts: A review, Catalysis Today. 154 (2010) 162–182. https://doi.org/10.1016/j.cattod.2010.02.077.
[14] L. van de Water, G. Bezemer, J. Bergwerff, M. Versluijs-Helder, B. Weckhuysen, K. de Jong, Spatially resolved UV–vis microspectroscopy on the preparation of alumina-supported Co Fischer–Tropsch catalysts: Linking activity to Co distribution and speciation, Journal of Catalysis. 242 (2006) 287–298. https://doi.org/10.1016/j.jcat.2006.06.004.
[15] J.-B. d'Espinose de Lacaillerie, M. Kermarec, O. Clause, Impregnation of gamma-Alumina with Ni (II) or Co (II) Ions at Neutral pH: Hydrotalcite-Type Coprecipitate Formation and Characterization, Journal of the American Chemical Society. 117 (1995) 11471–11481.
[16] J.-F. Lambert, M. Che, The molecular approach to supported catalysts synthesis: state of the art and future challenges, Journal of Molecular Catalysis A: Chemical. 162 (2000) 5–18. https://doi.org/10.1016/S1381-1169(00)00318-6.
[17] K. Larmier, C. Chizallet, P. Raybaud, Tuning the Metal-Support Interaction by Structural Recognition of Cobalt-Based Catalyst Precursors, Angewandte Chemie International Edition. 54 (2015) 6824–6827. https://doi.org/10.1002/anie.201502069.
[18] T. Yang, M. Ehara, Probing the electronic structures of Co_n (n = 1–5) clusters on γ-Al_2O_3 surfaces using first-principles calculations, Phys. Chem. Chem. Phys. 19 (2017) 3679–3687. https://doi.org/10.1039/C6CP06785A.
[19] A.S. Andreev, M.A. Kazakova, A. V. Ishchenko, A.G. Selyutin, O.B. Lapina, V.L. Kuznetsov, J.-B. d'Espinose de Lacaillerie, Magnetic and dielectric properties of carbon nanotubes with embedded cobalt nanoparticles, Carbon. 114 (2017) 39–49. https://doi.org/10.1016/j.carbon.2016.11.070.
[20] M.A. Kazakova, A.S. Andreev, A.G. Selyutin, A. V. Ishchenko, A. V. Shuvaev, V.L. Kuznetsov, O.B. Lapina, J.-B. d'Espinose de Lacaillerie, Co metal nanoparticles deposition inside or outside multi-walled carbon nanotubes via facile support pretreatment, Applied Surface Science. 456 (2018) 657–665. https://doi.org/10.1016/j.apsusc.2018.06.124.

[21] I.V. Yakovlev, S.S. Yakushkin, M.A. Kazakova, S.N. Trukhan, Z.N. Volkova, A.P. Gerashchenko, A.S. Andreev, A.V. Ishchenko, O.N. Martyanov, O.B. Lapina, J.-B. d'Espinose de Lacaillerie, Superparamagnetic behaviour of metallic Co nanoparticles according to variable temperature magnetic resonance, Phys. Chem. Chem. Phys. 23 (2021) 2723–2730. https://doi.org/10.1039/D0CP05963C.

[22] A.S. Andreev, D.V. Krasnikov, V.I. Zaikovskii, S.V. Cherepanova, M.A. Kazakova, O.B. Lapina, V.L. Kuznetsov, J. d'Espinose de Lacaillerie, Internal field ^{59}Co NMR study of cobalt-iron nanoparticles during the activation of $CoFe_2/CaO$ catalyst for carbon nanotube synthesis, Journal of Catalysis. 358 (2018) 62–70. https://doi.org/10.1016/j.jcat.2017.11.025.

[23] A.C. Gossard, A.M. Portis, M. Rubinstein, R.H. Lindquist, Ferromagnetic Nuclear Resonance of Single-Domain Cobalt Particles, Physical Review. 138 (1965) A1415–A1421. https://doi.org/10.1103/PhysRev.138.A1415.

[24] V. V. Matveev, D.A. Baranov, G.Yu. Yurkov, N.G. Akatiev, I.P. Dotsenko, S.P. Gubin, Cobalt nanoparticles with preferential hcp structure: A confirmation by X-ray diffraction and NMR, Chemical Physics Letters. 422 (2006) 402–405. https://doi.org/10.1016/j.cplett.2006.02.099.

[25] A.S. Andreev, O.B. Lapina, S.V. Cherepanova, A New Insight into Cobalt Metal Powder Internal Field^{59}Co NMR Spectra, Applied Magnetic Resonance. 45 (2014) 1009-1017. https://doi.org/10.1007/s00723-014-0580-0.

[26] A.S. Andreev, J.-B. D'Espinose De Lacaillerie, O.B. Lapina, A. Gerashenko, Thermal stability and hcp-fcc allotropic transformation in supported Co metal catalysts probed near operando by ferromagnetic NMR, Physical Chemistry Chemical Physics. 17 (2015) 14598-14604. https://doi.org/10.1039/c4cp05327c.

[27] Y. Liu, J. Luo, Y. Shin, S. Moldovan, O. Ersen, A. Hébraud, G. Schlatter, C. Pham-Huu, C. Meny, Sampling the structure and chemical order in assemblies of ferromagnetic nanoparticles by nuclear magnetic resonance, Nature Communications. 7 (2016) 11532. https://doi.org/10.1038/ncomms11532.

[28] K. Pansanga, J. Panpranot, O. Mekasuwandumrong, C. Satayaprasert, J.G. Goodwin, P. Praserthdam, Effect of mixed γ- and χ-crystalline phases in nanocrystalline Al_2O_3 on the dispersion of cobalt on Al_2O_3, Catalysis Communications. 9 (2008) 207–212. https://doi.org/10.1016/j.catcom.2007.05.042.

[29] R. Prins, On the structure of γ-Al_2O_3, Journal of Catalysis. 392 (2020) 336–346. https://doi.org/10.1016/j.jcat.2020.10.010.

[30] S. V Tsybulya, G.N. Kryukova, Nanocrystalline transition aluminas: Nanostructure and features of x-ray powder diffraction patterns of low-temperature Al_2O_3 polymorphs, Physical Review B. 77 (2008) 24112. https://doi.org/10.1103/PhysRevB.77.024112.

[31] D.F. Khabibulin, E. Papulovskiy, A.S. Andreev, A.A. Shubin, A.M. Volodin, G.A. Zenkovets, D.A. Yatsenko, S.V. Tsybulya, O.B. Lapina, Surface Hydroxyl OH Defects of η-Al_2O_3 and χ-Al_2O_3 by Solid State NMR, XRD, and

DFT Calculations, Zeitschrift Für Physikalische Chemie. 231 (2017) 809–825. https://doi.org/10.1515/zpch-2016-0822.
[32] L. Favaro, A. Boumaza, P. Roy, J. Lédion, G. Sattonnay, J.B. Brubach, A.M. Huntz, R. Tétot, Experimental and ab initio infrared study of χ-, κ- and α-aluminas formed from gibbsite, Journal of Solid State Chemistry. 183 (2010) 901–908. https://doi.org/10.1016/j.jssc.2010.02.010.
[33] S.A. Yashnik, A.V. Ishchenko, L.S. Dovlitova, Z.R. Ismagilov, The Nature of Synergetic Effect of Manganese Oxide and Platinum in Pt–MnO_X–Alumina Oxidation Catalysts, Top Catal. 60 (2017) 52–72. https://doi.org/10.1007/s11244-016-0722-8.
[34] S.A. Yashnik, V.V. Kuznetsov, Z.R. Ismagilov, Effect of χ-alumina addition on H_2S oxidation properties of pure and modified γ-alumina, Chinese Journal of Catalysis. 39 (2018) 258–274. https://doi.org/10.1016/S1872-2067(18)63016-5.
[35] D.A. Nazimov, O.V. Klimov, I.G. Danilova, S.N. Trukhan, A.V. Saiko, S.V. Cherepanova, Yu.A. Chesalov, O.N. Martyanov, A.S. Noskov, Effect of alumina polymorph on the dehydrogenation activity of supported chromia/alumina catalysts, Journal of Catalysis. 391 (2020) 35–47. https://doi.org/10.1016/j.jcat.2020.08.006.
[36] K. Pansanga, J. Panpranot, O. Mekasuwandumrong, C. Satayaprasert, J.G. Goodwin, P. Praserthdam, Effect of mixed γ- and χ-crystalline phases in nanocrystalline Al_2O_3 on the dispersion of cobalt on Al_2O_3, Catalysis Communications. 9 (2008) 207–212. https://doi.org/10.1016/j.catcom.2007.05.042.
[37] I. V. Yakovlev, A.M. Volodin, V.O. Stoyanovskii, O.B. Lapina, A.F. Bedilo, Effect of carbon coating on the thermal stability of nanocrystalline χ-Al_2O_3, Materials Chemistry and Physics. 240 (2020) 122135. https://doi.org/10.1016/j.matchemphys.2019.122135.
[38] I. V. Yakovlev, A.M. Volodin, V.I. Zaikovskii, V.O. Stoyanovskii, O.B. Lapina, A.A. Vedyagin, Stabilizing effect of the carbon shell on phase transformation of the nanocrystalline alumina particles, Ceramics International. 44 (2018) 4801–4806. https://doi.org/10.1016/j.ceramint.2017.12.066.
[39] P. Panissod, J.P. Jay, C. Meny, M. Wojcik, E. Jedryka, NMR analysis of buried metallic interfaces, Hyperfine Interact. 97–98 (1996) 75–98. https://doi.org/10.1007/BF02150169.
[40] J.R. Yates, C.J. Pickard, F. Mauri, Calculation of NMR chemical shifts for extended systems using ultrasoft pseudopotentials, Physical Review B. 76 (2007) 024401. https://doi.org/10.1103/PhysRevB.76.024401.
[41] P.E. Blöchl, Projector augmented-wave method, Physical Review B. 50 (1994) 17953–17979. https://doi.org/10.1103/PhysRevB.50.17953.
[42] J.P. Perdew, J.A. Chevary, S.H. Vosko, K.A. Jackson, M.R. Pederson, D.J. Singh, C. Fiolhais, Atoms, molecules, solids, and surfaces: Applications of the

generalized gradient approximation for exchange and correlation, Physical Review B. 46 (1992) 6671–6687. https://doi.org/10.1103/PhysRevB.46.6671.
[43] B.G. Pfrommer, M. Côté, S.G. Louie, M.L. Cohen, Relaxation of Crystals with the Quasi-Newton Method, Journal of Computational Physics. 131 (1997) 233–240. https://doi.org/10.1006/jcph.1996.5612.
[44] S.J. Clark, M.D. Segall, C.J. Pickard, P.J. Hasnip, M.I.J. Probert, K. Refson, M.C. Payne, First principles methods using CASTEP, Zeitschrift Für Kristallographie - Crystalline Materials. 220 (2005) 567–570. https://doi.org/10.1524/zkri.220.5.567.65075.
[45] J.P. Perdew, K. Burke, M. Ernzerhof, Generalized Gradient Approximation Made Simple, Physical Review Letters. 77 (1996) 3865–3868. https://doi.org/10.1103/PhysRevLett.77.3865.
[46] D. Vanderbilt, Soft self-consistent pseudopotentials in a generalized eigenvalue formalism, Physical Review B. 41 (1990) 7892–7895. https://doi.org/10.1103/PhysRevB.41.7892.
[47] M.F. Hansen, S. Mørup, Models for the dynamics of interacting magnetic nanoparticles, Journal of Magnetism and Magnetic Materials. 184 (1998) L262-274. https://doi.org/10.1016/S0304-8853(97)01165-7.
[48] D.L. Leslie-Pelecky, R.D. Rieke, Magnetic Properties of Nanostructured Materials, Chem. Mater. 8 (1996) 1770–1783. https://doi.org/10.1021/cm960077f.
[49] O. Kitakami, H. Sato, Y. Shimada, F. Sato, M. Tanaka, Size effect on the crystal phase of cobalt fine particles, Phys. Rev. B. 56 (1997) 13849–13854. https://doi.org/10.1103/PhysRevB.56.13849.
[50] G. Mattei, C. de Julián Fernández, P. Mazzoldi, C. Sada, G. De, G. Battaglin, C. Sangregorio, D. Gatteschi, Synthesis, Structure, and Magnetic Properties of Co, Ni, and Co−Ni Alloy Nanocluster−Doped SiO_2 Films by Sol−Gel Processing, Chem. Mater. 14 (2002) 3440–3447. https://doi.org/10.1021/cm021106r.
[51] W. Sucksmith, The magnetic anisotropy of cobalt, Proc. R. Soc. Lond. A. 225 (1954) 362–375. https://doi.org/10.1098/rspa.1954.0209.
[52] C. Chizallet, C. Schlaup, E. Fonda, X. Carrier, Surface orientation dependent interaction of cobalt (II) precursors with alpha-alumina, Journal of Catalysis. 394 (2021) 157–166. https://doi.org/10.1016/j.jcat.2020.10.025.
[53] G. Busca, The surface of transitional aluminas: A critical review, Catalysis Today. 226 (2014) 2–13. https://doi.org/10.1016/j.cattod.2013.08.003.
[54] H. Knözinger, P. Ratnasamy, Catalytic Aluminas: Surface Models and Characterization of Surface Sites, Catalysis Reviews. 17 (1978) 31–70. https://doi.org/10.1080/03602457808080878.
[55] M. Digne, P. Sautet, P. Raybaud, P. Euzen, H. Toulhoat, Hydroxyl Groups on γ-Alumina Surfaces: A DFT Study, Journal of Catalysis. 211 (2002) 1–5. https://doi.org/10.1006/jcat.2002.3741.

[56] M. Digne, Use of DFT to achieve a rational understanding of acid-basic properties of γ-alumina surfaces, Journal of Catalysis. 226 (2004) 54–68. https://doi.org/10.1016/j.jcat.2004.04.020.
[57] X. Krokidis, P. Raybaud, A.-E. Gobichon, B. Rebours, P. Euzen, H. Toulhoat, Theoretical Study of the Dehydration Process of Boehmite to γ-Alumina, J. Phys. Chem. B. 105 (2001) 5121–5130. https://doi.org/10.1021/jp0038310.
[58] A.T.F. Batista, D. Wisser, T. Pigeon, D. Gajan, F. Diehl, M. Rivallan, L. Catita, A.-S. Gay, A. Lesage, C. Chizallet, P. Raybaud, Beyond γ-Al_2O_3 crystallite surfaces: The hidden features of edges revealed by solid-state ^1H NMR and DFT calculations, J. Catal. 378 (2019) 140–143. https://doi.org/10.1016/j.jcat.2019.08.009.
[59] T. Pigeon, C. Chizallet, P. Raybaud, Revisiting γ-alumina surface models through the topotactic transformation of boehmite surfaces, J. Catal. 405 (2022) 140–151. https://doi.org/10.1016/j.jcat.2021.11.011.
[60] H.C. Stumpf, A.S. Russell, J.W. Newsome, C.M. Tucker, Thermal Transformations of Aluminas and Alumina Hydrates - Reaction with 44% Technical Acid., Ind. Eng. Chem. 42 (1950) 1398–1403. https://doi.org/10.1021/ie50487a039.
[61] V.P. Pakharukova, D.A. Yatsenko, E.Y. Gerasimov, S.V. Tsybulya, A study of γ-Al_2O_3 from the viewpoint of 3D nanostructure, Journal of Solid State Chemistry. 302 (2021) 122425. https://doi.org/10.1016/j.jssc.2021.122425.
[62] C.V. Chandran, C.E.A. Kirschhock, S. Radhakrishnan, F. Taulelle, J.A. Martens, E. Breynaert, Alumina: discriminative analysis using 3D correlation of solid-state NMR parameters, Chem. Soc. Rev. 48 (2019) 134–156. https://doi.org/10.1039/C8CS00321A.
[63] D.A. Yatsenko, V.P. Pakharukova, S.V. Tsybulya, Low Temperature Transitional Aluminas: Structure Specifics and Related X-ray Diffraction Features, Crystals. 11 (2021) 690. https://doi.org/10.3390/cryst11060690.
[64] D.A. Ksenofontov, Yu.K. Kabalov, Structure refinement and thermal stability of gibbsite, Inorg. Mater. 48 (2012) 142–144. https://doi.org/10.1134/S0020168512020136.
[65] J.M.R. Mercury, P. Pena, A.H. de Aza, D. Sheptyakov, X. Turrillas, On the Decomposition of Synthetic Gibbsite Studied by Neutron Thermodiffractometry, J. Am. Ceram. Soc. 89 (2006) 3728–3733. https://doi.org/10.1111/j.1551-2916.2006.01191.x.
[66] T. Mitsui, T. Matsui, R. Kikuchi, K. Eguchi, Microstructural Transformation with Heat-Treatment of Aluminum Hydroxide with Gibbsite Structure, Bull. Chem. Soc. Jpn. 82 (2009) 618–623. https://doi.org/10.1246/bcsj.82.618.
[67] M. Salmeron, H. Bluhm, M. Tatarkhanov, G. Ketteler, T.K. Shimizu, A. Mugarza, X. Deng, T. Herranz, S. Yamamoto, A. Nilsson, Water growth on metals and oxides: binding, dissociation and role of hydroxyl groups, Faraday Discuss. 141 (2009) 221–229. https://doi.org/10.1039/B806516K.

[68] X. Deng, T. Herranz, C. Weis, H. Bluhm, M. Salmeron, Adsorption of Water on Cu_2O and Al_2O_3 Thin Films, J. Phys. Chem. C. 112 (2008) 9668–9672. https://doi.org/10.1021/jp800944r.